inorganics

MDPI

Article

The Impact of Supramolecular Forces on the Magnetic and Optical Properties of Bis(2-amino-6-bromopyridinium) Tetrachloridocuprate $(C_5H_6BrN_2)_2[CuCl_4]$

Lokmen Ghorbali [1], Vladimir Kjartan Stojadinovic [2], Axel Klein [2,*] and Hammouda Chebbi [1,3,*]

[1] Laboratory of Materials, Crystal Chemistry and Applied Thermodynamics, Faculty of Sciences of Tunis, University of Tunis El Manar, El Manar II, Tunis 2092, Tunisia; lokmen.ghorbali@gmail.com
[2] Department of Chemistry and Biochemistry, Institute for Inorganic and Materials Chemistry, Faculty of Mathematics and Natural Sciences, University of Cologne, Greinstraße 6, D-50939 Köln, Germany; vstojadi@smail.uni-koeln.de
[3] Preparatory Institute for Engineering Studies of Tunis, University of Tunis, Jawaharlal Nehru Street, Montfleury, Tunis 1089, Tunisia
* Correspondence: axel.klein@uni-koeln.de (A.K.); chebbhamouda@yahoo.fr (H.C.)

Abstract

The organic/inorganic hybrid compound bis(2-amino-6-bromopyridinium) tetrachloridocuprate(II) $(HABPy)_2[CuCl_4]$ was synthesized in crystalline form in a 77% yield from aqueous HCl solutions containing $Cu(OAc)_2$ and 2-amino-6-bromopyridine (ABPy). Single-crystal X-ray diffraction analysis revealed that the compound crystallizes in the monoclinic, centrosymmetric space group *C*2/c. The Cu atom shows a distorted tetrahedral coordination geometry with a τ_4 value of 0.69 (τ_4 = 1 for a perfect tetrahedron). The structure consists of organic $(HABPy)^+$ cation layers at z = 0 and z = ½, alternating with inorganic $[CuCl_4]^{2-}$ dianion layers at z = ¼ and z = ¾. These layers, parallel to the (001) plane, are interconnected by a plethora of supramolecular forces such as N–H···Cl hydrogen bonds, forming a three-dimensional network. Powder X-ray diffraction confirmed the purity of the synthesized bulk material. Fourier-transform infrared (FT-IR) spectroscopy and Raman spectroscopy support the protonation of the pyridine N atom. Hirshfeld surface analysis allowed us to further study the supramolecular forces in the crystal structure. The material shows purely paramagnetic behavior according to S = ½ with an effective magnetic moment μ_{eff} of 1.85 μB and a g factor of 2.14, in keeping with magnetically isolated $[CuCl_4]^{2-}$ dianions. UV-vis diffuse reflectance spectroscopy of the orange-red material showed a tiny band at 314 nm and an intense band peaking at 622 nm. The optical gap was found to be 2.25 eV. The photoluminescence spectrum shows a partially structured band with maxima at 416 and 436 nm when irradiating at 370 nm, the wavelength of the maximum band found in the excitation spectrum.

Keywords: 2-amino-6-bromopyridinium; tetrachloridocuprate(II); isomeric structures; supramolecular interactions; optical properties; magnetic susceptibility

check for updates

Academic Editors: Wanlu Li and Liping Xu

Received: 8 August 2025
Revised: 1 October 2025
Accepted: 10 October 2025
Published: 16 October 2025

Citation: Ghorbali, L.; Stojadinovic, V.K.; Klein, A.; Chebbi, H. The Impact of Supramolecular Forces on the Magnetic and Optical Properties of Bis(2-amino-6-bromopyridinium) Tetrachloridocuprate $(C_5H_6BrN_2)_2[CuCl_4]$. *Inorganics* **2025**, *13*, 339. https://doi.org/10.3390/inorganics13100339

1. Introduction

Organic/inorganic hybrid halidometalates $[(A)_n\{MX_m\}]_o$ (X = halides or pseudohalides), consisting of a 3D, 2D, or 1D halidometalate network or 0D insulate halidometalates and organic cations (Scheme 1), are an important subgroup of coordination polymers [1–11]. The most prominent examples are the so-called organic/inorganic (hybrid) perovskites, which have gained attention due to their intriguing optical and electronic properties, making them promising candidates for use in photovoltaic applications [3,4,10–15]. The prototypical example of a 3D perovskite arrangement is $MAPbI_3$ (MA = methylammonium), in which the MA^+ cation occupies the central A position in a classical AMX_3 perovskite structure with an anionic ${}^{3}_{\infty}\{MX_3\}^-$ scaffold (Scheme 1, 3D) [3,4,12,15,16].

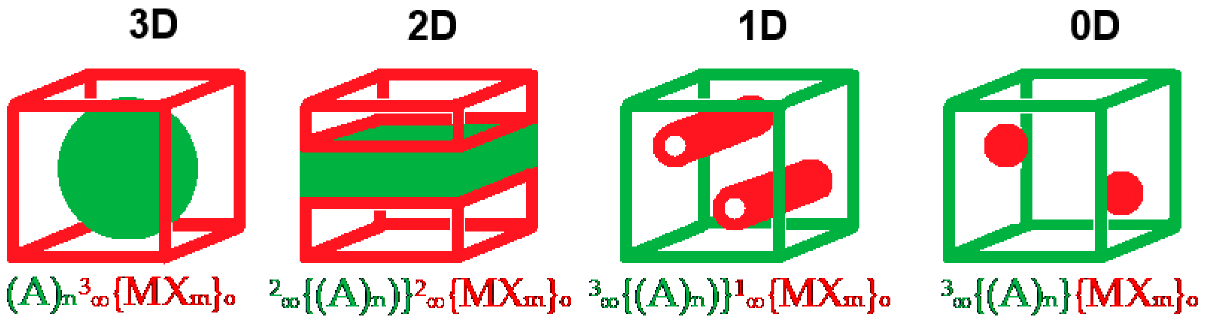

Scheme 1. Sketch of 3D, 2D, 1D, and 0D halidometalates $\{MX_m\}^{n-}$ (in red) with organic cations or cation networks (in green).

In 2D variants, ${}^{2}_{\infty}\{MX_m\}_o^{n-}$ layers are interleaved with ${}^{2}_{\infty}\{A\}^{n+}$ cation layers (Scheme 1, **2D**), produced from bulkier organic bases and acids. The organic cations in the layer might be interconnected through weak forces such as $\pi\cdots\pi$-stacking, hydrogen bonding, or van der Waals interactions. Many of these 2D materials retain the typical perovskite properties, especially the (photo)semiconducting ability [4,5,9–11,17]. Corresponding 1D materials (Scheme 1, **1D**) containing ${}^{1}_{\infty}\{MX_m\}_o^{n-}$ chains and the so-called "zero-dimensional (0D) perovskites" containing isolated halidometalates $\{MX_m\}^{n-}$ hardly parallel true perovskite structures but some of these materials exhibit very interesting optical and magnetic properties [5,6,11,18–20]. The cations in these 1D and 0D structures might be arranged in a 3D network of cations ${}^{3}_{\infty}\{A\}^{n+}$, but again, the intercationic forces are weak.

From a coordination chemistry perspective, the above-described classification including 0D materials is reasonable and can be very useful, as the simplest synthesis method, the crystallization from solutions containing metal halides, organic bases such as amines or pyridines, and acids (HX), might lead to materials that can be classified using the dimension of the containing halidometalate. The challenge for the synthesis and structuring of corresponding 1D and 0D materials lies in the design of the organic cations aiming to use supramolecular forces such as hydrogen bonding, π-stacking, halogen bonds, dipolar, or apolar van der Waals interactions, either between the halidometalates and the organic cations or between the cations, in addition to the electrostatic forces between cationic and anionic entities. To this end, bi- or polyfunctional organic bases containing a function for protonation along with other functional groups for coordination, hydrogen bonding, or other supramolecular forces have been introduced [11,14,17–24]. Many of these bases are (hetero)aromatic molecules providing additional electronic absorption properties [11,14,21–29].

Cu(II), with its interesting magnetic (Cu^{2+} has a d^9 configuration with an unpaired electron) and optical properties (intense green to blue absorptions from ligand field transitions for octahedral or orange-red absorptions for tetrahedral configurations) in combination with a very flexible coordination behavior (coordination numbers vary from 4 to 6), has become the focus of research devoted to organic/inorganic hybrid materials [11,16,25,30–41], expanding the range of metals beyond Pb(II), Sn(II), Bi(III), and Sb(III) [1,3,5,10,11,14–16,18,20]. Cu(II)-containing 3D perovskites have been reported, such as the chlorides MA_2MCl_4 [30] and the formiate $MA[Cu(HCOO)_3]$ (MA = methylammonium) [32]. However, low-dimensional structures are more frequent for Cu(II) [9,25,33–39], such as the chiral ferromagnets (*R*-MPEA)$_2$[CuCl$_4$] and (*S*-MPEA)$_2$[CuCl$_4$] (MPEA = β-methylphenethylamine) [36], as well as isolated tetrahalidocuprates [25,42–59].

From the idea that heteroaromatic cations might be beneficial for the electronic properties of organic/inorganic hybrid materials, pyridine-containing organic bases have been vastly used in the design of low-dimensional Cu(II)-containing organic/inorganic hybrid materials [25,35,42–45,47–58], with aminopyridines being quite frequent among them for the versatile ditopic pyridine N + amine N combination [42,43,45,50–54,56,57,59]. However, the aforementioned simple synthesis from Cu(II) salts, pyridines, and acid might not only yield the desired salt-like pyridinium halidocuprates but also lead to Cu pyridine complexes [25,39,60–65]. Moreover, prediction of the dimensionality of the resulting pyridinium halidocuprates is almost impossible, especially if additional functionalities on the pyridine fostering further supramolecular forces come into play.

Amino-bromo-pyridines are good examples of polyfunctional pyridines designed for supramolecular forces (Scheme 2), but only 2-amino-5-bromo-pyridine has to date been used in organic/inorganic halido Cu(II)-based materials [43,52,57,64]. The pyridine function is the most basic and will be protonated in the presence of acids forming pyridinium cations. Alternatively, in unprotonated form, the pyridine N atom might coordinate yielding pyridine complexes, as was found for the complex *trans*-[CuCl$_2$(5ABPy)$_2$] of the isomeric 2-amino-5-bromo-pyridine (5ABPy) [65].

Scheme 2. Functional groups in 2-amino-6-bromo-pyridine (ABPy) and the previously used 2-amino-5-bromo-pyridine isomer.

The amino function in aminopyridines might be additionally protonated at very low pH values, but it can also coordinate, thus allowing the formation of coordination polymers. Alternatively, the NH$_2$ function might serve as hydrogen bond acceptor (N) or donor (H) in hydrogen bonding networks. The bromo substituent might serve for the formation of halogen bonds, play a role through its bulkiness, or simply have an impact on the dipolar moment of the molecule. Additionally, Br-substitution at the ortho-position lowers the basicity of the pyridine N atom. From this it is clear that the placing of the bromo and amino function makes the four 2-amino-bromo-pyridines quite different molecules.

An interesting aspect studies is the impact of different isomers of such bi- or trifunctional pyridines on the structures of the resulting materials, especially on the dimensionality and supramolecular features, and consequently on the magnetic properties and the photophysics of such organic/inorganic hybrid materials [35,43,47,51–53,57–60].

In this study, we report on the 0D organic/inorganic hybrid material bis(2-amino-6-bromopyridinium) tetrachloridocuprate(II) (HABPy)$_2$[CuCl$_4$], synthesized from Cu(OAc)$_2$ and 2-amino-6-bromopyridine in the presence of hydrochloric acid in aqueous solution in high yields. The crystal structure from single-crystal X-ray diffraction and Hirshfeld surface analyses together with Raman and Fourier-transform infrared (FT-IR) spectroscopy shows multiple supramolecular interactions. Magnetic susceptibility, UV-vis absorption, diffuse reflectance, and photoluminescence spectroscopy were employed to investigate the optical properties of the new material.

2. Results and Discussion

2.1. Synthesis of (HABPy)$_2$[CuCl$_4$]

Orange crystalline material of the compound was obtained in a 77% yield from a 1:2 mixture of Cu(OAc)$_2$ and 6-bromo-2-pyridine in water at a pH of 1 using hydrochloric acid. The acid provides the chloride ions for the tetrachloridocuprate dianion and protonates the 6-bromo-2-pyridine, thus making it soluble in water as pyridinium cation (6-bromo-2-pyridine itself is insoluble in water). Elemental analysis agreed with the calculated values for $C_{10}H_{12}Br_2N_4CuCl_4$ (553.39 g/mol); see Section 2.3. Powder X-ray diffraction of the bulk material showed good agreement with the calculated pattern (Figure S1). FT-IR and Raman spectra are discussed below. Remarkably, while the mixture of CuCl$_2$ and 2-amino-5-bromopyridine gave the Cu(II) complex *trans*-[CuCl$_2$(5ABPy)$_2$] in a 85% yield from a MeOH solution [65], we found no evidence for a complex such as [CuCl$_2$(ABPy)$_2$]; instead, we isolated the material (HABPy)$_2$[CuCl$_4$] in a good yield. This is probably due to the two *ortho* substituents NH$_2$ and Br shielding the pyridine N atom against coordination.

2.2. Structural Analysis

The title compound crystallizes in the triclinic space group *C*2/c (structure solution and refinement data in Table S1, Supplementary Materials, SM). The projection of the crystal packing in the [100] direction reveals an alternation of anionic and cationic layers (Figure 1). The asymmetric unit consists of a half tetrahedral anion [CuCl$_4$]$^{2-}$ and one protonated (HABPy)$^+$ cation (Figure 2).

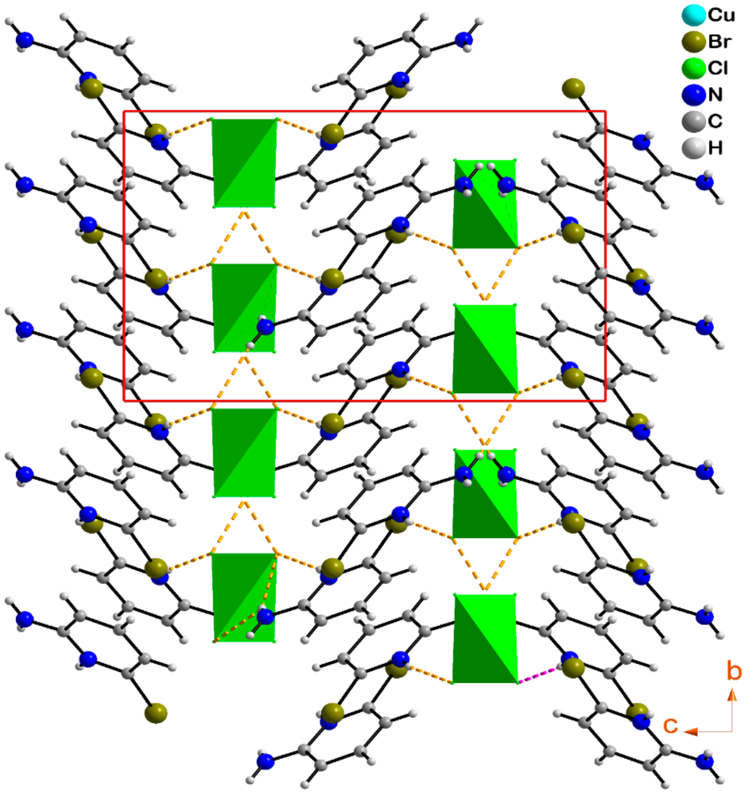

Figure 1. Projection along the [100] direction of the (HABPy)$_2$[CuCl$_4$] structure showing alternating organic and inorganic layers.

The Cu atom is located on a twofold rotation axis which results in a special position with the fractional coordinates 0.5, 0.68, and 0.25. The two other Cl atoms in the [CuCl$_4$]$^{2-}$ tetrahedron are generated through the (1–x, y, 1/2–z) symmetry operation. The Cu atom is coordinated by four chlorido ligands with Cu–Cl bond lengths of 2.211(3) and 2.287(3) Å and Cl–Cu–Cl angles ranging from 98.0(1) to 131.0(1)° (Figure S2 and Table S2, SM). These values differ markedly from an ideal tetrahedral configuration. The τ_4 value of the title structure is 0.69, as calculated from θ = 109.5° and from the two largest angles around Cu, α and β (Equation (1)).

$$\tau_4 = \frac{360^\circ - (\alpha + \beta)}{360^\circ - 2\theta} \tag{1}$$

A τ_4 value of 1 represents a perfect tetrahedral geometry, while a value of 0 represents a surrounding square planar. The τ_4 value of 0.69 represents a flattened tetrahedral structure typical for previously reported structures for this ion (Table 1) [56,59,66,67]. This is also the reason for the well-studied thermochromism of tetrachloridocuprates(II), which is interpreted as a phase transition accompanied by a change in the coordination geometry from distorted tetrahedral to square planar with decreasing temperature [56,67–73].

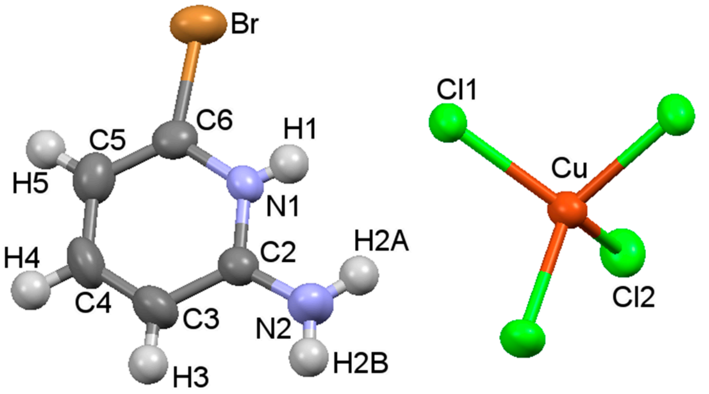

Figure 2. Molecular structures of the asymmetric unit of $(HABPy)_2[CuCl_4]$ with atom labeling.

Table 1. τ_4 values of the title compound compared to selected similar $A_2[CuCl_4]$ compounds [a].

A^+ Cation	Formulae	τ_4 Values	Reference
2-amino-6-bromopyridinium	$(C_5H_6BrN_2)_2[CuCl_4]$	0.69	this work
2-amino-5-bromopyridinium	$(C_5H_6BrN_2)_2[CuCl_4]$	0.57	[43]
3-amino-2-chloropyridinium	$(C_5H_6ClN_4)_2[CuCl_4]$	0.58	[54]
4-*tert*-butyl-pyridinium	$(C_9H_{14}N)_2[CuCl_4]$	0.58, 0.55 [a]	[44]
2-amino-5-methylpyridinium	$(C_6H_9N_2)_2[CuCl_4]$	0.57	[45]
1,4′-bipyridine-1,1′-diium	$(C_{10}H_{10}N_2)[CuCl_4]$	0.53	[47]
2-amino-4-methylpyridinium	$(C_6H_9N_2)_2[CuCl_4]$	0.48	[53]
2,2,6,6-tetramethylpiperidinium-1-yl)oxidanyl	$(C_9H_{19}NO)_2[CuCl_4]$	0.70	[48]
4-amino-2-methylpyridinium	$(C_6H_9N_2)_2[CuCl_4]$	0.44	[51]
4-amino-2-chloropyridinium	$(C_5H_6ClN_2)_2[CuCl_4]$	0.62	[51]
2-methyl-pyridinium	$(C_6H_8N)_2[CuCl_4]$	0.67	[46]
4-dimethylamino-pyridinium	$(C_7H_{11}N_2)_2\ [CuCl_4]$ [b]	0.42/0.86	[56]

[a] Two independent $[CuCl_4]^{2-}$ anions in the structure. [b] Two polymorphs in $P\bar{1}$ (green) and $C2/c$ (yellow) space group are reported.

The varying τ_4 values shown in Table 1 can be discussed as the result of an energetic compromise between the lattice energy and the maximum bonding energy of the $[CuCl_4]^{2-}$ dianions in these structures. The variations suggest that the geometry of the $[CuCl_4]^{2-}$ dianion is flexible and tolerates flattening of the tetrahedral structure if this flattening enables more dense packing of the components in conjunction with non-covalent forces in the crystal structure, thus optimizing the lattice energy.

Within the non-covalent forces having impact on the $[CuCl_4]^{2-}$ geometry, hydrogen binding might play an important role. In $(HABPy)_2[CuCl_4]$, Cl1, $Cl2^i$, and $Cl1^i$ are hydrogen bond acceptors interconnecting the layers of dianions and cations in the structure, especially through N–H···Cl interactions (Figures 1 and S3). Both the pyridine hydrogen atoms (N1–H1···Cl1) and the amine H atoms (N2–H2A···Cl1, N2–H2A···$Cl2^i$ and N2–H2B···$Cl1^i$) contribute to this (Table S3). Additionally, there are a number of C–H···Cl contacts between the cations and the anions and C–H···Br contacts between cations of neighboring layers (Figure S4). The closest C–H···Cl contacts are 2.73(7) Å, and the closest C–H···Br is 3.63(1) Å. Table S3 shows that the N–H···Cl interactions range from about 2.5 to 2.7 Å. Taken together with their D–H···A angles, these are weak electrostatic interactions [74]. The same is true for the C–H···Cl and C–H···Br contacts, in addition to the point that C–H groups are poor hydrogen bond donors. But in summary, these hydrogen bonds might have an important impact on the structure.

The bromo substituents on the $HABPy^+$ cations pointing towards the $[CuCl_4]^{2-}$ dianions show Cl···Br contacts of 3.97(5) Å (Figure S4). They lie beyond the sum of van der Waals interactions of 3.66 Å [75] and probably do not markedly contribute to the lattice energy. The pyridinium ions exhibit pair-wise π···π-stacking interactions with a centroid distance of 3.86(4) Å, parallel offset, and the pyridine N atoms and Br substituents pointing away from each other (Figure S4). This is typical for π···π-stacking in N-containing heterocyclic aromatics [76]. The relatively long distance agrees with a moderate to weak strength of this interaction. So, it seems that the hydrogen bonding is essentially dominating the non-covalent forces in the crystal structure, besides the Coulomb interaction between dianions and the organic cations.

The distances and bond angles within the organic cations are given in Table S2. The protonation at the pyridine N atom is confirmed through the elongated C–N distance N1–C2 = 1.340(5) Å. In addition, the pyridinium cation shows a widened C2–N1–C6 angle of 122.9(3)°. Such widening of the C–N–C angle upon protonation has been reported in related structures [44–47,53]. The conjugation between the amine group and the pyridine ring is reflected in the relatively short N2–C2 = 1.334(5) Å bond of the amine group. The average C–C bond value within the pyridine moiety is 1.371(5) Å. The C–C–C angle values range from 117.8(4) to 122.4(4)° and are consistent with those reported in similar compounds containing the same cation [44–47,53].

2.3. Hirshfeld Surface Analysis

The Hirshfeld surface analysis of $(HABPy)_2[CuCl_4]$ in d_{norm} and shape index mode (Figure S5) confirm the N–H···Cl hydrogen bonding, while the shape index representation (Figure S5b) confirms the π···π interactions.

The 2D fingerprints of the Hirshfeld surface (Figure S6) show H···Cl/Cl···H contacts as two sharp peaks (top left and bottom right in Figure S6b) which are attributed mainly to the N–H···Cl hydrogen bonds and only in small part to the C–H···Cl interactions. With 47.8% they make the largest contribution to the total Hirshfeld surface (Figure S7), confirming their importance in the structure. H···Br/Br···H contacts contribute with 12.7% (Figure S6c), in line with the C–H···Br hydrogen bonds. The H···H contacts derived using $r^{vdw} = 1.20$ Å and $d_i \simeq d_e \simeq 1.4$ Å make up 8.8% of the total intermolecular contacts (Figure S6d). The H···C/C···H contacts account for 8.4% of all contacts and can be related to the π-stacking. The Br···Cl/Cl···Br interactions account for 5.7% of the interaction, while Br···Br interactions represent 1.5%. Further minor contributions to the Hirshfeld surface are Cl···C/C···Cl (3.9%), N···Cl/Cl···N (2.8%), H···Cu/Cu···H (2.5%), C···C (1.6%), N···H/H···N (1.2%), N···C/C···N (1%), Cu···Br/Br···Cu (0.7%), Br···C/C···Br (0.6%), N···Br/Br···N (0.5%), and N···N (0.3%) (Figure S7, Table S4). The Hirshfeld analysis thus supports the assumption that hydrogen bonding with an overall contribution of more than 60% of the total surface is the prevalent non-covalent force in the structure of (HABPy)$_2$[CuCl$_4$] besides Coulomb attraction.

2.4. Fourier-Transform Infrared (FT-IR) and Raman Spectroscopy

The FT-IR spectrum of (HABPy)$_2$[CuCl$_4$] (Figure 3) shows bands representing the vibrational modes of the 2-amino-6-bromo-pyridinium cations. They can be assigned based on comparison with similar compounds [43,49,54]. The bands in the ranges 3400–3100 cm^{-1} and 3085–2917 cm^{-1} represent the asymmetric and symmetric N–H and C–H stretching modes, respectively. The bands at 1655, 1590, 1532, and 1447 cm^{-1} stem from the pyridine ring modes. The band at 538 cm^{-1} is attributed to C–Br stretching. C–H out-of-plane deformations and the δ(C–C–C) and δ(C–C–N) modes are detected at 681–566 cm^{-1}.

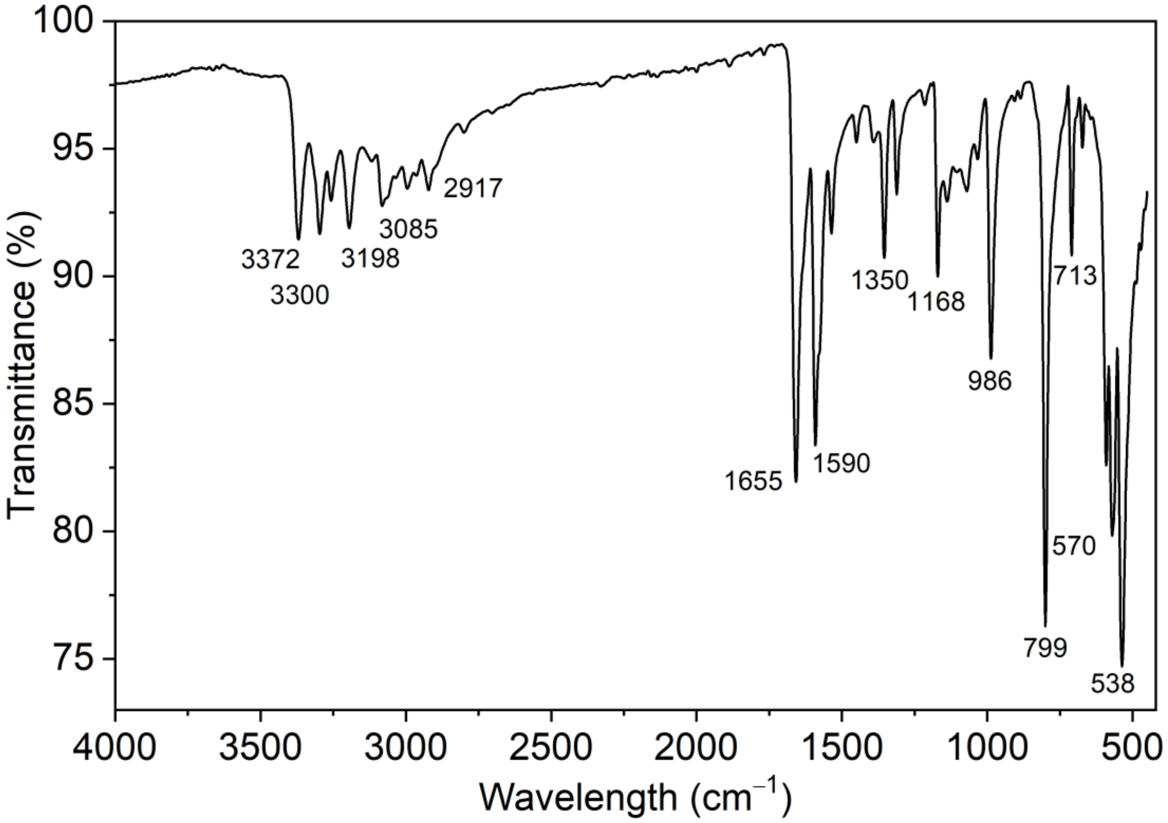

Figure 3. FT-IR spectrum of a bulk pellet sample of (HABPy)$_2$[CuCl$_4$]. IR spectrum of 2-amino-6-Br-Py (ABPy) in KBr can be found at https://www.chemicalbook.com/SpectrumEN_19798-81-3_IR1.htm, accessed on 7 August 2025.

The Raman spectrum (Figure 4) confirms the resonances that are typical for the pyridinium cation, found already in the FT-IR. In addition to them, four distinct bands were found at 305, 236, 160, and 119 cm$^{\hat{R}1}$, which represent the vibrational modes of the [CuCl$_4$]$^{2-}$ dianion [49,50,58,70,71] . Our data agree with a geometry between square planar and tetrahedral, but with a tendency towards tetrahedral, in keeping with the τ_4 value of 0.69.

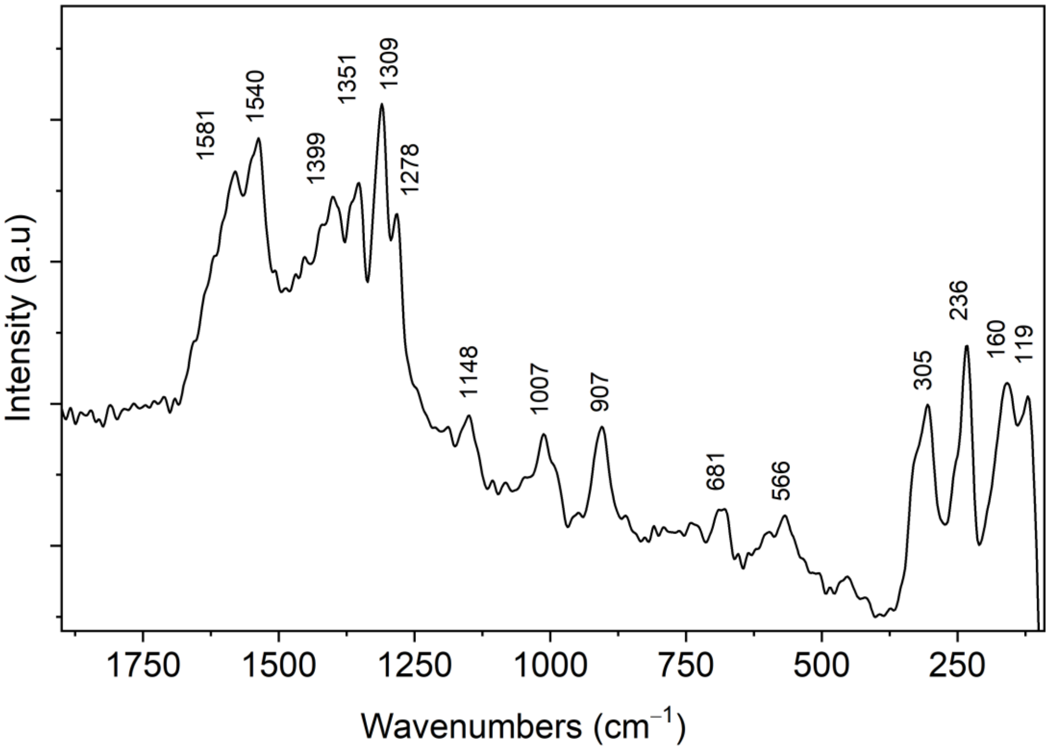

Figure 4. Raman spectrum of a bulk pellet sample of $(HABPy)_2[CuCl_4]$.

2.5. UV-Vis Diffuse Reflectance and Photoluminescence Spectroscopy

The UV-vis diffuse reflectance spectrum (DRS) of a thin solid sample of $(HABPy)_2[CuCl_4]$ shows maxima at 314 and 622 nm (Figure 5).

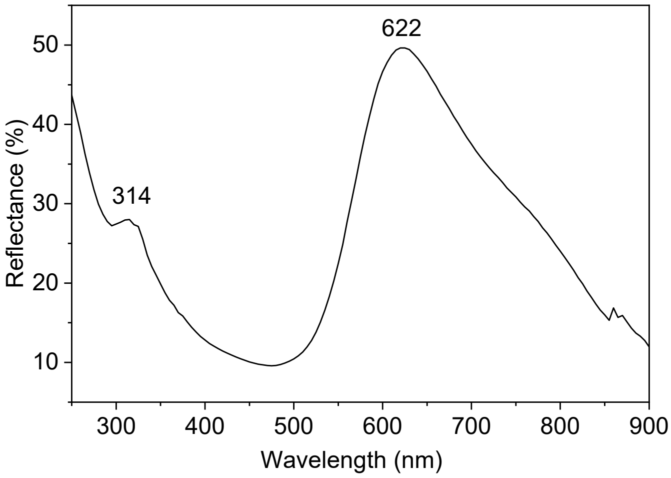

Figure 5. Solid-state UV-vis diffuse reflectance spectrum of $(HABPy)_2[CuCl_4]$ at 298 K.

The band at 314 nm is very probably associated with a ligand(Cl-p)-to-metal(Cu-d) charge transfer (LMCT) transition in keeping with similar reports [72,73] , while the $\pi \longrightarrow \pi^*$ transition in the 2-amino-6-bromopyridinium is expected at a lower wavelength < 300 nm and was not observed. For 2-amino-6-bromo-pyridine in MeCN, we recorded an absorption spectrum showing intense bands at 298, 239, and 197 nm (Figure S8) that correspond to $\pi \longrightarrow \pi^*$ transitions, supporting the LMCT assignment for the 317 nm band.

The long-wavelength band at 622 nm (~2 eV) refers to a d–d* transition in the flattened tetrahedral Cu^{2+} ion. In a perfect tetrahedral configuration this is the $e \longrightarrow t_2$ transition, while for flattened geometries the e and t_2 orbitals split into b_2 + e und b_1 + a_1, respectively [66]. Alternatively, the absorption can be associated with a ligand(Cl)-to-metal(Cu_d) charge transfer (LMCT) transition [72,73].

Solid $(NEt_2H_2)_2[CuCl_4]$ is reported to show an absorption maximum at 590 nm at 293 K, which shifted to 652 at 314 K [72] . The authors describe the high-T phase as yellow, while the low-T phase is described as deep green. Both phases adopt $P2_1/c$ symmetry; in both structures, approximated tetrahedral and approximated square planar $[CuCl_4]^{2-}$ structures coexist, but they differ in their ratio. The high-T phase shows a markedly higher degree of tetrahedral geometries. The orange color of $(NMe_4)_2[CuCl_4]$ crystal is related to absorptions at 1.5–2.2 eV (830–565 nm) [73].

Remarkably, our assignment to $\pi \longrightarrow \pi^*$ for the 314 nm band and d $\longrightarrow$ d* transition for the 622 nm band reflect a more or less molecular-type behavior and not a band-like electronic structure. This is consistent with other compounds containing the $[CuCl_4]^{2-}$ anion, including the butylammonium [38], bis(2,2,6,6–tetramethylpiperidinium-1-yl)oxidanyl (TEMPO-H^+) [48], 2-amino-5-methylpyridinium [45], and 4-*tert*-butyl-pyridinium salts [44], and is in line with the isolated $[CuCl_4]^{2-}$ units in these structures. Nevertheless, it is clear that there is a band structure underneath these electronic transitions. This can be seen when comparing our bands with those of (2-amino-5-methylpyridinium)$_2[CuCl_4]$ found at 316 and 519 nm [45]. While the energies are quite similar, the intensity of the two peaks are completely reversed, while for the 4-*tert*-butyl-pyridinium derivative, the peaks at 350 and 580 nm [42] show the same intensity ratio as our compound.

It is interesting to note that in the diffuse reflectance spectrum of the Cu(II) complex *trans*-$[CuCl_2(5ABPy)_2]$, bands at 720, 270, and 257 nm were observed. The 257 nm band was assigned to π–π^* transitions, the 270 nm absorption to a Cl-to-Cu LMCT transition, and the 720 nm band to the d–d* transition of the square planar configured complex [65]. This confirms our assignments for the 620 nm and 314 nm bands in $(HABPy)_2[CuCl_4]$. The optical gap energy can be approached through the Kubelka–Munk function [77] , extrapolating the slope of $(F(R)\ hv)^2$ to zero (Figure S9). Thus, the determined band gap energy of the solid material was about 2.25 eV.

When irradiating at 300 nm, the photoluminescence spectrum shows a partially structured emission band with maxima at 414 and 436 nm, and a shoulder at 467 nm (Figure 6). The excitation spectrum shows a broad band peaking at 370 nm, which accounts for a Stokes shift of 2875 cm^{-1}. We thus tentatively suggest that the emission occurs from an excited singlet ^{1}LMCT state.

A similar emission spectrum was reported for $(TEMPO\text{-}H)_2[CuCl_4]$, with a broad band peaking at 552 nm when irradiated at 385 nm [48]. For the 2-amino-5-methylpyridinium derivative two maxima at 433 and 472 nm (λ_{exc} = 290 nm) were observed and assigned to an LMCT excited state [45]. For butylammonium tetrachloridocuprate, an emission band at 442 nm was found, when irradiated at 380 nm [38]. As for the latter the butylammonium is unquestionably not responsible for this emission: the $[CuCl_4]^{2-}$ core must be the origin of the photoluminescence, confirming an LMCT assignment. However, to fully understand the photoluminescence, further measurements are necessary and in addition, the band structure of the title compound should be calculated. Furthermore, as the database for such ammonium or pyridinium tetrachloridocuprates is very small, with only a few examples [38,45,48], some further derivatives should be synthesized to allow drawing structure properties relations. This will be conducted in future work.

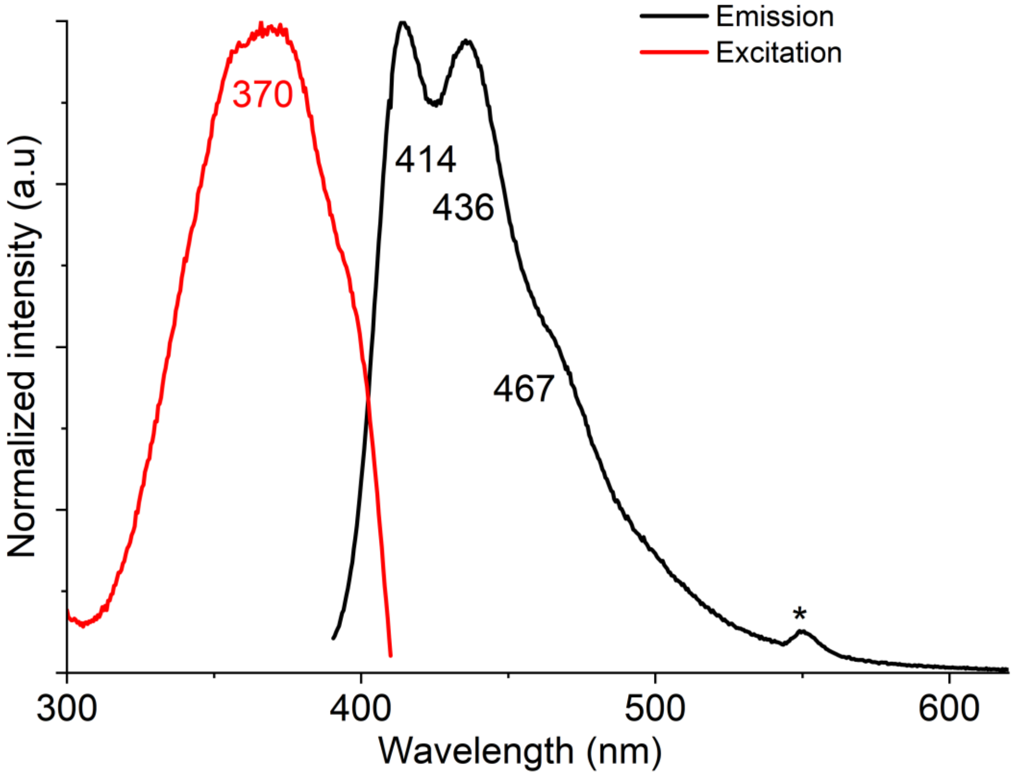

Figure 6. Photoluminescence spectra of solid $(HABPy)_2[CuCl_4]$, emission spectrum (black) for an excitation at λ_{ex} = 370 nm; excitation spectrum (red) for an emission wavelength λ_{em} = 435 nm. The asterisk * marks an artifact from the instrument.

2.6. Magnetic Susceptibility

The molar magnetic susceptibility χ of $(HABPy)_2[CuCl_4]$ follows the typical paramagnetic increase with decreasing temperature and there are no indications of any kind of magnetic order or correlations, as is most clearly seen by considering the inverse susceptibility which follows a straight line starting from the origin (Curie–Weiss fit with θ = +0.5 K, estimated uncertainty = ±1 K) (Figure 7). From the slope of this line, we derived effective magnetic moments $\mu_{eff} = g(S(S+1))^{1/2}$ μB of 1.85 μB, which for a spin S = ½ correspond to a g value of 2.14, which is a typical value for S = ½ Cu^{2+} ions with their $3d^9$ configuration [35,43,51,62].

Thus, the magnetic data reveal purely paramagnetic behavior of $(HABPy)_2[CuCl_4]$ ($C2/c$) and thus stand in contrast to the layered S = ½ Heisenberg antiferromagnets $(H5ABPy)_2[CuBr_4]$ (H5ABPy = 2-amino-5-bromopyridinium; space group $C2/c$) [57] and $(HAClPy)_2[CuBr_4]$ ($P\bar{1}$) (AClPy = 3-amino-2-chloropyridinium), or the magnetism of $(HAClPy)_2[CuCl_4]$ ($P\bar{1}$) [54] or $(H_2DAP)[CuBr_4]$ (DAP = hexahydrodiazepine) ($C2/c$) [40], that were fitted to an antiferromagnetic chain model. For $(H5ABPy)_2[CuCl_4]$ ($P\bar{1}$) a moderate antiferromagnetic interaction was found and fitted to an alternating chain model [43]. For (1,4′-bipyridine)-1,10-diium)$[CuCl_4]$ ($C2/c$) [47] very weak antiferromagnetic behavior was reported. As in the case of the two HAClPy-containing compounds, the antiferromagnetic interaction was stronger for the (1,4′-bipyridine)-1,10-diium)$[CuBr_4]$ ($C2/c$) compared to the $[CuCl_4]$ derivative [47]. All these structures contain isolated halidocuprates $[CuX_4]^{2-}$ but differ slightly in their halide···halide distances and orientation of the cations.

What becomes clear from this overview is that the structure predicts the magnetic properties, but the structure is not easy to predict [51]. So, using further amino-bromo-pyridine isomers in chlorido or bromido cuprates in future work might be a worthwhile endeavor.

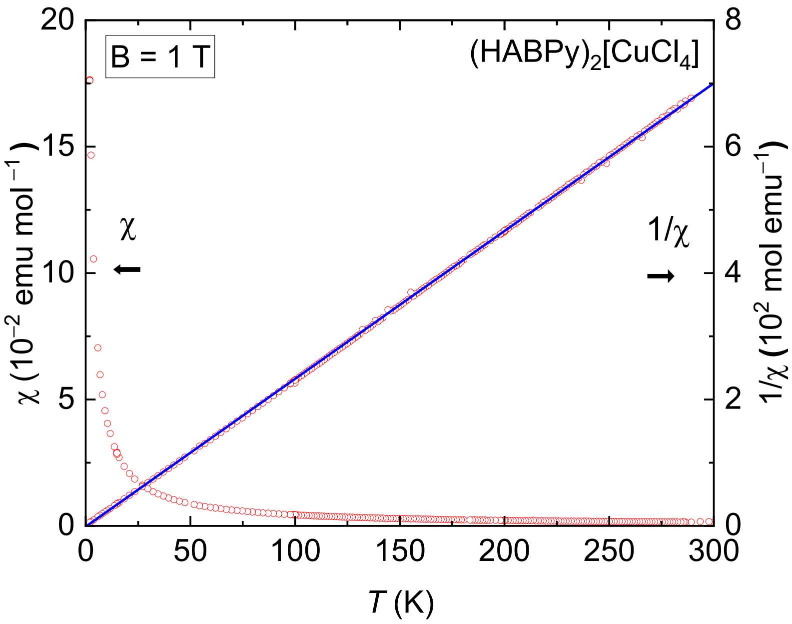

Figure 7. Molar magnetic susceptibility χ and $1/\chi$ over temperature T for $(HABPy)_2[CuCl_4]$ measured at a field of 1 T and Curie–Weiss fit (straight blue line) with $\theta = +0.5$ K (estimated uncertainty = ±1 K).

3. Materials and Methods

3.1. Materials

Reagents and solvents were obtained from sources and used without further purification: copper acetate ($Cu(OAc)_2$, 99%: Merck, Darmstadt, Germany), hydrochloric acid (HCl, 36%, Sigma-Aldrich, Merck, Darmstadt, Germany), and 6-bromo-2-aminopyridine ($C_5H_5BrN_2$, $\geq$98%, Sigma-Aldrich, Merck).

3.2. Instrumentation

Powder X-ray diffraction experiments were carried out using a Bruker D8 Advance (Bruker, Rheinhausen, Germany) with Cu Kα radiation ($\lambda = 1.5406$ Å). Data were collected at 298 K over a 2θ range of 5–50° with a step-width of 0.01° and an integration time of 1.5 s per step. The Fourier-transform infrared (FT-IR) spectra were recorded in the range 4000 to 400 cm^{-1} on a Perkin Elmer Spectrum Two UATR Two FT-IR spectrometer (PerkinElmer, Waltham, MA, USA), using pellets of the bulk material. Raman spectra were obtained at room temperature in the range 2000 to 100 cm^{-1} using a Jobin Yvon T6400 spectrometer (Horiba, Kyoto, Japan) equipped with a 488 nm argon laser excitation source. Optical reflectance spectra in the range 800 to 250 nm were measured at 298 K using a Perkin Elmer lambda 900 spectrometer (PerkinElmer, Waltham, MA, USA). UV-vis absorption spectra were recorded in water using a Double Beam UVD-3500 spectrophotometer (Labomed, Shandong, China). Photoluminescence spectra of the solid material were obtained using an LS55 Perkin Elmer spectrometer (PerkinElmer, Waltham, MA, USA) at an excitation wavelength of 300 nm.

3.3. Synthesis of $(HABPy)_2[CuCl_4]$

$(HABPy)_2[CuCl_4]$ was obtained from a mixture of 0.136 g (0.75 mmol) of $Cu(OAc)_2$ and 0.252 g of 6-bromo-2-aminopyridine (1.45 mmol) suspended in 30 mL of water acidified to a pH of 1 using hydrochloric acid. The reaction mixture was heated to 50 °C while stirring for about two hours until a clear blue solution was obtained. Then the solution was left standing at ambient temperature. After four days of slow evaporation at room temperature, orange crystals of suitable size for the structural study (powder and single-crystal XRD) were obtained. After a further six days, a total amount of 321 mg (0.58 mmol, 77%, based on $Cu(OAc)_2$) microcrystalline material was obtained and air-dried. Elemental analysis calc. (found) for $C_{10}H_{12}Br_2N_4CuCl_4$, 553.39 g/mol, in %: C 21.70 (21.77), H 2.19 (2.20), N 10.12 (10.11). FT-IR (pellet of the bulk material, in cm^{-1}): 3372 s, 3300 s, 3198 s, 3085 m, 2981 m, 2917 m, 1655 vs, 1590 vs, 1532 s, 1447 w, 1350 s, 1310 m, 1168 s, 1050 w, 986 vs, 907 w, 799 vs, 713 s, 600 m, 570 s, 538 vs. Raman (pellet of the bulk material, in cm^{-1}): 1581, 1540, 1399, 1351, 1309, 1278, 1148, 1007, 907, 681 566, 305, 236, 160, 119. UV-vis (solid, λ in nm): 314, 622.

3.4. Single-Crystal X-Ray Diffraction

An orange single crystal of $(HABPy)_2[CuCl_4]$ was selected and used for X-ray diffraction experiments. Diffraction intensities were collected using an Enraf-Nonius CAD4 four-circle diffractometer (Delft Instruments B.V., Delft, The Netherlands) with Mo-Kα radiation (λ = 0.71067 Å). The raw data processing was carried out using the XCAD4 program [78]. The structure was solved by direct methods using the SHELXT-2018/3 program [79] and refined through full-matrix least squares methods on all F^2 data using the program SHELXL-2018/3 [80] . Crystal data, data collection, and structure refinement details are summarized in Table S1. Hydrogen atoms are attached using the HFIX instruction with C–H distances 0.93 Å (aromatic), with $U_{iso}(H) = 1.2\ U_{eq}(C)$. The H atoms on the amino group (NH_2) and the pyridinium N–H function were located from the difference Fourier map and isotropically refined. Anisotropic thermal parameters were used to refine all the non-hydrogen atoms. The full structural information is deposited in Cambridge Crystallographic Data Centre (CCDC 2182468) and freely available upon request from the following website: https://www.ccdc.cam.ac.uk/data_request/cif, accessed on 7 August 2025.

3.5. Magnetic Measurements

The magnetic susceptibility was measured in an MPMS Quantum Design SQUID magnetometer (Quantum Design, Pfungstadt, Germany) applying an external field of 1 Tesla in the temperature range from 300 K down to 2 K by using the so-called DC measurement mode. A small capsule that was fixed inside the center of a drinking straw and mounted to the magnetometer was filled with 36 mg of the powdered sample. The capsule produced an essentially T-independent diamagnetic background signal that needs to be subtracted from the raw data to obtain the powder susceptibilities, which at room temperature are only about twice as large as the background signal. However, with decreasing temperature the powder susceptibilities rapidly increase and exceed the background signal by more than one or two orders of magnitude below 100 K and 10 K, respectively.

4. Conclusions

The reaction of 2-amino-6-bromopyridine (ABPy) with $Cu(OAc)_2$ in aqueous HCl solution (pH = 1) gave the pyridinium salt bis(2-amino-6-bromopyridinium) tetrachloridocuprate(II) $(HABPy)_2[CuCl_4]$ in a yield of 77% with no other isolable by-products. $(HABPy)_2[CuCl_4]$ crystallized in the monoclinic space group $C2/c$. The crystal packing shows a plethora of supramolecular forces such as N–H···Cl and C–H···Cl hydrogen bonding, and Br···Cl interactions between the layers of the $HABPy^+$ cations and the layers of $[CuCl_4]^{2-}$. Within the layers of the cations, π···π-stacking of two pyridinium units is found. These interactions were confirmed through Hirshfeld surface and topological analysis. Remarkably, the major part, almost 50%, of the Hirshfeld surface represents H···Cl/Cl···H contacts, and overall the hydrogen bonding has the largest impact on the structure among the non-covalent and non-ionic forces, with more than 60% contribution to the Hirshfeld surface. They very probably are also an important factor for the flattening of the $[CuCl_4]^{2-}$ dianions, with a τ_4 value of 0.69. Magnetic susceptibility measurements revealed purely paramagnetic behavior of $(HABPy)_2[CuCl_4]$, with a μ_{eff} of 1.85 μB, which for a spin S of ½, corresponds to a g value of 2.14, a typical value for Cu^{2+} ions with their $3d^9$ configuration. Thus, the supramolecular forces described above rather separate the magnetic $[CuCl_4]^{2-}$ dianions from each other, allowing not even the tiniest magnetic interaction. The UV-vis diffuse reflectance spectrum showing a broad band peaking at 622 nm which is assigned to the d $\longrightarrow$ d* transition and a smaller band at 314 nm assignable to an LMCT transition confirms that the $[CuCl_4]^{2-}$ chromophores are rather isolated in the structure. When irradiating at 370 nm, the photoluminescence spectrum shows a partially structured emission with maxima at 416 and 436 nm. The underlying excited state is probably of a ligand(Cl)-to-metal(Cu) charge transfer (^{1}LMCT) character.

Supplementary Materials: The following supporting information can be downloaded at https://www.mdpi.com/article/10.3390/inorganics13100339/s1: Figure S1: Superposition of the experimental powder X-ray diffractogram and the calculated diffractogram based on the single-crystal structure of $(HABPy)_2[CuCl_4]$; Figure S2: Bond length (Å) and bond angles (°) around the $[CuCl_4]^{2-}$ anion; Figure S3: Selected N–H···Cl hydrogen bond metrics in $(HABPy)_2[CuCl_4]$; Figure S4: View of the crystal structure of $(HABPy)_2[CuCl_4]$ showing $\pi\cdots\pi$, Cl···Br, H···Br, and H···Cl interactions; Figure S5: Hirshfeld surface of $(HABPy)_2[CuCl_4]$ in d_{norm} mode and shape index mode; Figure S6: Hirshfeld surface analysis 2D fingerprint plots with the main interactions; Figure S7: Hirshfeld surface analysis, total contributions to intermolecular contacts; Figure S8: UV-vis absorption spectrum of 2-amino-6-bromopyridine in MeCN; Figure S9: Tauc plot = extrapolation of the Kubelka–Munk function $(F(R)\,h\upsilon)^2$ to zero giving the energy gap; Table S1: Selected structure solution and refinement data for $(HABPy)_2[CuCl_4]$; Table S2: Bond metrics in $(HABPy)_2[CuCl_4]$; Table S3: Hydrogen bond geometries in $(HABPy)_2[CuCl_4]$; Table S4: Relative contributions of intermolecular contacts to the Hirshfeld surface area in $(HABPy)_2[CuCl_4]$.

Author Contributions: Investigation, L.G. and V.K.S.; Supervision, H.C. and A.K.; Writing—original draft, L.G. and H.C.; Revision, A.K. All authors have read and agreed to the published version of the manuscript.

Funding: This research received no external funding.

Institutional Review Board Statement: Not applicable.

Informed Consent Statement: Not applicable.

Data Availability Statement: The original contributions presented in this study are included in the article/supplementary material. Further inquiries can be directed to the corresponding authors.

Acknowledgments: The Laboratory of Applied Mineral Chemistry, Faculty of Sciences of Tunis, University of Tunis El Manar, is acknowledged for the FT-IR measurements. The Common Research Services Unit, Department of Physics, Faculty of Sciences of Tunis, University of Tunis El Manar, is acknowledged for Raman and optical measurements. Tobias Lapic, Department of Chemistry and Biochemistry, University of Cologne, is acknowledged for assisting with photoluminescence spectra. Special thanks go to Fatma Garci and Mohamed Faouzi Zid for collecting single-crystal X-ray data. Thomas Lorenz, Department of Physics, University of Cologne, is acknowledged for the magnetic measurements.

Conflicts of Interest: The authors declare no conflicts of interest.

References

1. Schlachter, A.; Tanner, K.; Harvey, P.D. Copper halide-chalcogenoether and -chalcogenone networks: Chain and cluster motifs, polymer dimensionality and photophysical properties. *Coord. Chem. Rev.* **2021**, *448*, 214176. [CrossRef]
2. Englert, U. Halide-bridged polymers of divalent metals with donor ligands—Structures and properties. *Coord. Chem. Rev.* **2010**, *254*, 537–554. [CrossRef]
3. Zhou, K.; Qi, B.; Liu, Z.; Wang, X.; Sun, Y.; Zhang, L. Advanced Organic–Inorganic Hybrid Materials for Optoelectronic Applications. *Adv. Funct. Mater.* **2024**, *34*, 2411671. [CrossRef]

4. Zheng, H.; Loh, K.P. Ferroics in Hybrid Organic–Inorganic Perovskites: Fundamentals, Design Strategies, and Implementation. *Adv. Mater.* **2024**, *36*, 2308051. [CrossRef]
5. Zhou, C.; Xu, L.-J.; Lee, S.; Lin, H.; Ma, B. Recent Advances in Luminescent Zero-Dimensional Organic Metal Halide Hybrids. *Adv. Opt. Mater.* **2021**, *9*, 2001766. [CrossRef]
6. Li, M.; Xia, Z. Recent progress of zero-dimensional luminescent metal halides. *Chem. Soc. Rev.* **2021**, *50*, 2626–2662. [CrossRef]
7. Niu, T.; Xue, Q.; Yip, H.-L. Advances in Dion-Jacobson phase two-dimensional metal halide perovskite solar cells. *Nanophotonics* **2021**, *10*, 2069–2102. [CrossRef]
8. Katan, C.; Mercier, N.; Even, J. Quantum and Dielectric Confinement Effects in Lower-Dimensional Hybrid Perovskite Semiconductors. *Chem. Rev.* **2019**, *119*, 3140–3192. [CrossRef]
9. Mao, L.; Stoumpos, C.C.; Kanatzidis, M.G. Two-Dimensional Hybrid Halide Perovskites: Principles and Promises. *J. Am. Chem. Soc.* **2019**, *141*, 1171–1190. [CrossRef]
10. Theofylaktos, L.; Kosmatos, K.O.; Giannakaki, E.; Kourti, H.; Deligiannis, D.; Konstantakou, M.; Stergiopoulos, T. Perovskites with d-block metals for solar energy applications. *Dalton Trans.* **2019**, *48*, 9516–9537. [CrossRef]
11. Saparov, B.; Mitzi, D.B. Organic−Inorganic Perovskites: Structural Versatility for Functional Materials Design. *Chem. Rev.* **2016**, *116*, 4558–4596. [CrossRef]
12. Feng, S.; Wang, J. Prediction of Organic–Inorganic Hybrid Perovskite Band Gap by Multiple Machine Learning Algorithms. *Molecules* **2024**, *29*, 499. [CrossRef]
13. Wang, Y.P.; Li, H.C.; Huang, Y.C.; Tan, C.S. Synthesis and Applications of Halide Perovskite Nanocrystals in Optoelectronics. *Inorganics* **2023**, *11*, 39. [CrossRef]
14. Coccia, C.; Moroni, M.; Malavasi, L. Chiral Metal Halide Perovskites: Focus on Lead-Free Materials and Structure-Property Correlations. *Molecules* **2023**, *28*, 6166. [CrossRef] [PubMed]
15. Ünlü, F.; Jung, E.; Öz, S.; Choi, H.; Fischer, T.; Mathur, S. Chemical Processing of Mixed-Cation Hybrid Perovskites: Stabilizing Effects of Configurational Entropy. In *Perovskite Solar Cells: Materials, Processes, and Devices*, 1st ed.; Ahmad, S., Kazim, S., Grätzel, M., Eds.; Chapter 1; WILEY-VCH GmbH: Weinheim, Germany, 2022; pp. 1–31, ISBN 978-3-527-34715-5.
16. Chatterjee, S.; Pal, A.J. Influence of metal substitution on hybrid halide perovskites: Towards lead-free perovskite solar cells. *J. Mater. Chem. A* **2018**, *6*, 3793–3823. [CrossRef]
17. Cui, F.; García-López, V.; Wang, Z.; Luo, Z.; He, D.; Feng, X.; Dong, R.; Wang, X. Two-Dimensional Organic−Inorganic van der Waals Hybrids. *Chem. Rev.* **2025**, *125*, 445–520. [CrossRef]
18. Han, L.; Wang, P.; Wang, Z.; Liu, Y.; Zheng, Z.; Cheng, H.; Huang, B. Zero-dimensional hydrazine iodobismuthate as a lead-free perovskite-like light absorber in a self-powered photodetector. *J. Alloys Compd.* **2022**, *893*, 162347. [CrossRef]
19. Zhou, J.; Yun, X.Y.; Fang, C.; Xu, D.H.; Li, X.; Cui, Y.Y.; Zhang, Z.C. Ternary zero-dimensional hybrid metal halides with dual emission. *Mater. Today Chem.* **2022**, *23*, 100757. [CrossRef]
20. Yu, T.; Mao, X.; Xu, X.; Wang, Z.; Zhang, R. Ultrafast dynamics of a highly-emissive zero-dimensional organic tin bromide perovskite. *Chem. Phys. Lett.* **2021**, *769*, 138411. [CrossRef]
21. Vijayakanth, T.; Liptrot, D.J.; Gazit, E.; Boomishankar, R.; Bowen, C.R. Recent Advances in Organic and Organic–Inorganic Hybrid Materials for Piezoelectric Mechanical Energy Harvesting. *Adv. Funct. Mater.* **2022**, *32*, 2109492. [CrossRef]
22. Novikov, A.S. Non-Covalent Interactions in Organic, Organometallic, and Inorganic Supramolecular Systems Relevant for Medicine, Materials Science, and Catalysis. *Crystals* **2022**, *12*, 246. [CrossRef]
23. Speetzen, E.D.; Nwachukwu, C.I.; Bowling, N.P.; Bosch, E. Complementary, Cooperative Ditopic Halogen Bonding and Electron Donor-Acceptor π-π Complexation in the Formation of Cocrystals. *Molecules* **2022**, *27*, 1527. [CrossRef]
24. Shen, Y.; Hu, S.; Meng, Y.; Yip, S.P.; Ho, J.C. Aromatic spacer engineering for 2D halide perovskites and their application in solar cells. *Mater. Today Electron.* **2024**, *8*, 100100. [CrossRef]
25. Klein, A.; Krakor, S.; Payen, L.; Walleriu, C. Azo- and Hydrazo-Dipyridines in Halidometallate Structures. *Inorg. Chem. Res.* **2024**, *7*, 65–75. [CrossRef]
26. Selivanov, N.I.; Rozhkova, Y.A.; Kevorkyants, R.; Emeline, A.V.; Bahnemann, D.W. The effect of organic cations on the electronic, optical and luminescence properties of 1D piperidinium, pyridinium, and 3-hydroxypyridinium lead trihalides. *Dalton Trans.* **2020**, *49*, 4390–4403. [CrossRef] [PubMed]
27. Van Gompel, W.T.M.; Herckens, R.; Van Hecke, K.; Ruttens, B.; D'Haen, J.; Lutsen, L.; Vanderzande, D. Low-Dimensional Hybrid Perovskites Containing an Organic Cation with an Extended Conjugated System: Tuning the Excitonic Absorption Features. *Chem. Nanomater. Energy Biol. More* **2019**, *5*, 323–327. [CrossRef]
28. García-Espejo, G.; Rodríguez-Padrón, D.; Pérez-Morales, M.; Luque, R.; de Miguel, G.; Camacho, L. Mechanochemical synthesis of one-dimensional (1D) hybrid perovskites incorporating polycyclic aromatic spacers: Highly fluorescent cation-based materials. *J. Mater. Chem. C* **2018**, *6*, 7677–7682. [CrossRef]
29. Ju, M.-G.; Dai, J.; Ma, L.; Zhou, Y.; Zeng, X.C. Zero-Dimensional Organic-Inorganic Perovskite Variant: Transition between Molecular and Solid Crystal. *J. Am. Chem. Soc.* **2018**, *140*, 10456–10463. [CrossRef]

30. Zhao, H.; Fu, H.; Hu, Z.; Fu, Q.; Tao, H.; Weng, J.; Xiong, L.; Cheng, Z. Magnetic hybrid organic–inorganic perovskite $(CH_3NH_3)_2XCl_4$ (X = Mn, Cu, Co) crystals. *CrystEngComm* **2021**, *23*, 5208–5213. [CrossRef]
31. Kusumoto, S.; Nagasawa, S.; Suzuki, R.; Tachibana, M.; Tsuji, T.; Zenno, H.; Nakashima, Y.; Hayami, S.; Kim, Y.; Koide, Y. Ferromagnetic and plastically deformable organic–inorganic hybrid crystal: $(C_7H_9NH_3)_2CuCl_4$, *Chem. Commun.* **2025**, *61*, 10303–10306. [CrossRef]
32. Baker, P.J.; Lancaster, T.; Franke, I.; Hayes, W.; Blundell, S.J.; Pratt, F.L.; Jain, P.; Wang, Z.-M.; Kurmoo, M. Muon spin relaxation investigation of magnetic ordering in the hybrid organic-inorganic perovskites $[(CH_3)_2NH_2]M(HCOO)_3$ (M = Ni, Co, Mn, Cu). *Phys. Rev. B* **2010**, *82*, 012407. [CrossRef]
33. Salgado-Pizarro, R.; Puigjaner, C.; Garcia, J.; Fernandez, A.I.; Barreneche, C. Copper- and manganese-based layered hybrid organic–inorganic compounds with polymorphic transitions as energy storage materials. *J. Mater. Chem. A* **2024**, *12*, 18544–18553. [CrossRef]
34. Topic, E.; Rubcic, M. Structural Insights into Layered Tetrahalocuprates(II) Based on Small Unsaturated and Cyclic Primary Ammonium Cations. *Materials* **2023**, *16*, 2236. [CrossRef]
35. Topić, E.; Senjug, P.; Barisic, D.; Loncaric, I.; Pajic, D.; Rubcic, M. Structure-Related Evolution of Magnetic Order in Anisidinium Tetrachlorocuprates(II). *Cryst. Growth Des.* **2023**, *23*, 4262–4272. [CrossRef]
36. Sun, B.; Liu, X.-F.; Li, X.-Y.; Zhang, Y.; Shao, X.; Yang, D.; Zhang, H.-L. Two-Dimensional Perovskite Chiral Ferromagnets. *Chem. Mater.* **2020**, *32*, 8914–8920. [CrossRef]
37. Ferreira, C.F.; Pérez-Cordero, E.E.; Abboud, K.A.; Talham, D.R. Reversible Medium-Dependent Solid–Solid Phase Transformations in Two-Dimensional Hybrid Perovskites. *Chem. Mater.* **2016**, *28*, 5522–5529. [CrossRef]
38. Xiao, Z.L.; Chen, H.Z.; Shi, M.M.; Wu, G.; Zhou, R.J.; Yang, Z.S.; Wang, M.; Tang, B.Z. Preparation and characterization of organic–inorganic hybrid perovskite $(C_4H_9NH_3)_2CuCl_4$. *Mater. Sci. Eng. B* **2005**, *117*, 313–316. [CrossRef]
39. Czugler, M.; Kotai, L.; Sreedhar, B.; Rockenbauer, A.; Gacs, I.; Holly, S. The Effect of HCl on the Copper(II) Chloride/Pyridine/Water System: Synthesis, Properties and Crystal Structure of $[(pyH)_2CuCl_4]$ and $[(pyH)_2Cu_3Cl_8(H_2O)_2]_n$. *Eur. J. Inorg. Chem.* **2002**, *2002*, 3298–3304. [CrossRef]
40. Bourwina, M.; Msalmi, R.; Walha, S.; Turnbull, M.M.; Roisnel, T.; Guesmi, A.; Houas, A.; Hamadi, N.B.; Naïli, H. Crystal Chemistry, Optic and Magnetic Characterizations of a New Copper Based Material Templated by Hexahydrodiazepine. *ACS Omega* **2023**, *8*, 15075–15082. [CrossRef]
41. Rogalewicz, B.; Szczesio, M.; Poleszak, E.; Kowalczyk, J.; Szewczyk, B.; Camargo, B.C.; Szczytko, J.; Witkowski, M.; Fruzinski, A.; Raducka, A.; et al. Influence of Incorporation of Different d^n-Electron Metal Cations into Biologically Active System on Its Biological and Physicochemical Properties. *Int. J. Mol. Sci.* **2021**, *22*, 12909. [CrossRef]
42. Li, Y.-T.; Huang, L.; Li, X.-R.; Hu, B.-Y.; Li, X.-L.; Jiang, Y.; Yu, J.-Y.; Ni, C.-L. Preparation, Crystal Structure, Optical Properties, Hirshfeld Surface Analysis and Antibacterial Activity of 4-Nitrobenzyl-4-aminopyridinium Tetrachlorocuprate(II). *J. Chem. Crystallogr.* **2024**, *54*, 291–304. [CrossRef]
43. Bedford, C.P.; Landee, C.P.; Wikaira, J.L.; Turnbull, M.M. Copper(II) halide salts of 5-bromo-2-aminopyridine and 3,5-dibromo-2-aminopyridine: Syntheses, structures and magnetic behavior. *J. Coord. Chem.* **2023**, *76*, 1353–1369. [CrossRef]
44. Althobaiti, M.G.; Hermi, S.; Alotaibi, A.A.; Alotaibi, K.M.; Hassan, H.A.; Mi, J.-X.; Ben Nasr, C.; Mrad, M.H. A New Cu(II) Metal Complex Template with 4-tert-Butyl-Pyridinium Organic Cation: Synthesis, Structure, Hirshfeld Surface, Characterizations and Antibacterial Activity. *Crystals* **2022**, *12*, 254. [CrossRef]
45. Gatfaoui, S.; Issaoui, N.; Noureddine, O.; Roisnel, T.; Marouani, H. Self assembly of a novel Cu(II) complex, $(C_6H_9N_2)_2[CuCl_4]$: Experimental, computational, and molecular docking survey. *J. Iran. Chem. Soc.* **2021**, *18*, 2331–2343. [CrossRef]
46. Mehmood, T.; Bhosale, R.S.; Reddy, J.P. Bis(2-methylpyridinium) tetrachloridocuprate(II): Synthesis, structure and Hirshfeld surface analysis. *Acta Crystallogr. E Res. Commun.* **2021**, *77*, 726–729. [CrossRef]
47. Monroe, J.C.; Landee, C.P.; Rademeyer, M.; Turnbull, M.M. Copper(II) Halide Salts with 1-(4′-Pyridyl)-Pyridinediium. *Inorganics* **2020**, *8*, 18. [CrossRef]
48. Ben Hmida, W.; Jellali, A.; Abid, H.; Hamdi, B.; Naili, H.; Zouari, R. Synthesis, crystal structure, vibrational studies, optical properties and DFT calculation of a new luminescent material based Cu(II). *J. Mol. Struct.* **2019**, *1184*, 604–614. [CrossRef]
49. Azouzi, K.; Hamdi, B.; Zouari, R.; Ben Salah, A. Crystal structure, Hirshfeld surface analysis, vibrational properties, and electrical and dielectric studies of the bis(4-benzylpyridinium) tetrachlorocuprate (II). *Ionics* **2016**, *22*, 1669–1680. [CrossRef]
50. Ben Nasr, M.; Lefebvre, F.; Ben Nasr, C. Synthesis, Crystal Structure and Infrared Characterization of Bis(4-dimethylamino-pyridinium) Tetrachlorocuprate. *Am. J. Anal. Chem.* **2015**, *6*, 446–456. [CrossRef]
51. Wikaira, J.L.; Landee, C.P.; Ludy, S.J.; Turnbull, M.M. Tetrahalocuprate salts of substituted 4-aminopyridines: Synthesis, structure and magnetic properties. *Polyhedron* **2013**, *52*, 770–780. [CrossRef]
52. Abdalrahman, M.A.; Awwadi, F.F.; Jameson, G.B.; Landee, C.P.; Saunders, C.G.; Turnbull, M.M.; Wikaira, J.L. Effects of halogen and hydrogen bonding on defect disorder: The ladder that wasn't there. *CrystEngComm.* **2013**, *15*, 4309–4320. [CrossRef]

53. Herringer, S.N.; Turnbull, M.M.; Landee, C.P.; Wikaira, J.L. Synthesis, structure, and magnetic properties of bis(3-amino-2-chloropyridinium)tetrahalocuprate(II) [halide = Cl or Br]. *J. Coord. Chem.* **2009**, *62*, 863–875. [CrossRef]
54. Al-Far, R.H.; Ali, B.F. Bis(2-amino-4-methyl pyridinium) tetrachloridocuprate(II). *Acta Crystallogr. E Crystal. Commun.* **2009**, *65*, m73. [CrossRef]
55. Haddad, S.F.; Al-Far, R.H. Crystal Structure of Three Isomorphous Compounds of 2,5-Dibromopyridine with Tetrahalometalate(II) Ions. *J. Chem. Crystallogr.* **2008**, *38*, 663–669. [CrossRef]
56. Haddad, S.; Willett, R.D. Polymorphism in Bis(4-dimethylamino-pyridinium)tetrachlorocuprate(II). *Inorg. Chem.* **2001**, *40*, 2457–2460. [CrossRef]
57. Woodward, F.M.; Landee, C.P.; Giantsidis, J.; Turnbull, M.M.; Richardson, C. Structure and magnetic properties of $(5BAP)_2CuBr_4$: Magneto-structural correlations of layered $S = 1/2$ Heisenberg antiferromagnets. *Inorg. Chim. Acta* **2001**, *324*, 324–330. [CrossRef]
58. Riley, M.J.; Boutchard, C.; Krausz, E.R.; Hitchman, M.A. Observation of a magnetic dipole origin in the spectrum of the square planar $CuCl_4^{2-}$ ion. *Chem. Phys. Lett.* **1996**, *254*, 403–409. [CrossRef]
59. Halvorson, K.E.; Patterson, C.; Willett, R.D. Structures of Bis(4-aminopyridinium) Tetrachlorocuprate(II) Monohydrate, $[C_5H_7N_2]_2[CuCl_4]\cdot H_2O$, and Bis(2-amino-3-hydroxypyridinium) Tetrachlorocuprate(II), $[C_5H_7N_2O]_2[CuCl_4]$: Correlation of $CuCl_4^{2-}$ Geometry with Hydrogen Bonding and Electronic Structure. *Acta Crystallogr. Sect. B Struct. Sci. Cryst. Eng. Mater.* **1990**, *46*, 508–519. [CrossRef]
60. Garci, F.; Chebbi, H.; Rouzbeh, N.; Rochels, L.; Disch, S.; Haseloer, A.; Sebastian, S.S.; Ruschewitz, U.; Anthony, E.T.; Klein, A.; et al. Structure, Optical and Magnetic Properties of Two Isomeric 2-Bromomethylpyridine Cu(II) Complexes $[Cu(C_6H_9NBr)_2(NO_3)_2]$ with Very Different Binding Motives. *Molecules* **2023**, *28*, 731. [CrossRef]
61. Hoffmann, C.; Kolks, N.; Smets, D.; Haseloer, A.; Gröner, B.; Urusova, E.A.; Endepols, H.; Neumaier, F.; Ruschewitz, U.; Klein, A.; et al. Next Generation Copper Mediators for the Efficient Production of ^{18}F-Labeled Aromatics. *Chem. Eur. J.* **2023**, *29*, e202202965. [CrossRef]
62. Wackerbarth, I.; Widhyadnyani, N.N.A.T.; Schmitz, S.; Stirnat, K.; Butsch, K.; Pantenburg, I.; Meyer, G.; Klein, A. Cu^{II} Complexes and Coordination Polymers with Pyridine or Pyrazine Amides and Amino Benzamides—Structures and EPR Patterns. *Inorganics* **2020**, *8*, 65. [CrossRef]
63. Bowmaker, G.A.; Di Nicola, C.; Pettinari, C.; Skelton, B.W.; Somers, N.; White, A.H. Mechanochemical synthesis in copper(II) halide/pyridine systems: Single crystal X-ray diffraction and IR spectroscopic studies. *Dalton Trans.* **2011**, *40*, 5102–5115. [CrossRef] [PubMed]
64. Luque, A.; Sertucha, J.; Lezama, L.; Rojo, T.; Román, P. Synthesis, characterisation and crystal structure of 2-aminopyridinium (2-amino-5-bromopyridine)tribromocuprate(II) and bis(2-aminopyridinium) tetrabromocuprate(II). *J. Chem. Soc. Dalton Trans.* **1997**, *1997*, 847–854. [CrossRef]
65. Ahmadi, R.A.; Hasanvand, F.; Bruno, G.; Rudbari, H.A.; Amani, S. Synthesis, Spectroscopy, and Magnetic Characterization of Copper(II) and Cobalt(II) Complexes with 2-Amino-5-bromopyridine as Ligand. *Russ. J. Coord. Chem.* **2013**, *39*, 867–871. [CrossRef]
66. Atanasov, M.; Ganyushin, D.; Sivalingam, K.; Neese, F. A Modern First-Principles View on Ligand Field Theory Through the Eyes of Correlated Multireference Wavefunctions. *Struct. Bond.* **2012**, *143*, 149–220. [CrossRef]
67. Ferguson, J. Electronic Absorption Spectrum and Structure of $CuCl_4^{2-}$. *J. Chem. Phys.* **1964**, *40*, 3406–3410. [CrossRef]
68. Winter, A.; Thiel, K.; Zabel, A.; Klamroth, T.; Pöppl, A.; Kelling, A.; Schilde, U.; Taubert, A.; Strauch, P. Tetrahalidocuprates(II)—Structure and EPR spectroscopy. Part 2: Tetrachloridocuprates(II). *New J. Chem.* **2014**, *38*, 1019–1030. [CrossRef]
69. Farra, R.; Thiel, K.; Winter, A.; Klamroth, T.; Pöppl, A.; Kelling, A.; Schilde, U.; Taubert, A.; Strauch, P. Tetrahalidocuprates(II)—Structure and EPR spectroscopy. Part 1: Tetrabromidocuprates(II). *New J. Chem.* **2011**, *35*, 2793–2803. [CrossRef]
70. Karoui, K.; Ben Bechir, M.; Bulou, A.; Guidara, K.; Ben Rhaiem, A. $[N(CH_3)_3H]_2CuCl_4$: Ab initio calculations and characterization of phase transitions by Raman spectroscopy. *J. Mol. Struct.* **2016**, *1114*, 161–170. [CrossRef]
71. Hitchman, M.A.; Cassidy, P.J. Polarized Crystal Spectrum of Bis(methylphenethylammonium) Tetrachlorocuprate(II): Analysis of the Energies, Vibrational Fine Structure, and Temperature Dependence of the “d-d” Transitions of the Planar $CuCl_4^{2-}$ Ion. *Inorg. Chem.* **1979**, *18*, 1745–1754. [CrossRef]
72. Kapustyanyk, V.B.; Korchak, Y.M. Thermochromic phase transition in $[NH_2(C_2H_5)_3]_2CuCl_4$ crystals. *J. Appl. Spectrosc.* **2000**, *67*, 1045–1049. [CrossRef]
73. Shymkiv, R.M.; Sveleba, S.A.; Karpa, I.V.; Katerynchuk, I.N.; Kunyo, I.M.; Phitsych, E.I. Electronic Spectra and Phase Transitions in Thin $[N(CH_3)_4]_2CuCl_4$ Microcrystals. *J. Appl. Spectr.* **2012**, *78*, 823–828. [CrossRef]
74. Steiner, T. The Hydrogen Bond in the Solid State. *Angew. Chem. Int. Ed.* **2002**, *41*, 48–76. [CrossRef]
75. Loy, C.; Zeller, M.; Rosokha, S.V. Halogen Bonding in the Complexes of Brominated Electrophiles with Chloride Anions: From a Weak Supramolecular Interaction to a Covalent Br–Cl Bond. *Crystals* **2020**, *10*, 1075. [CrossRef]
76. Janiak, C. A critical account on π–π stacking in metal complexes with aromatic nitrogen-containing ligands. *J. Chem. Soc. Dalton Trans.* **2000**, *2000*, 3885–3896. [CrossRef]

77. Kubelka, P.; Munk, F. Ein Beitrag zur Optik der Farbanstriche. *Z. Technol. Phys.* **1931**, *12*, 593–601, See Also English Translation by Westin, S. (An Article on Optics of Paint Layers). Available online: http://www.graphics.cornell.edu/~westin/pubs/kubelka.pdf (accessed on 8 August 2025).
78. Duisenberg, A.J.M. Indexing in Single-Crystal Diffractometry with an Obstinate List of Reflections. *J. Appl. Crystallogr.* **1992**, *25*, 92–96. [CrossRef]
79. Sheldrick, G.M. SHELXT—Integrated space-group and crystal-structure determination. *Acta Crystallogr. A Found. Adv.* **2015**, *71*, 3–8. [CrossRef]
80. Sheldrick, G.M. Crystal structure refinement with SHELXL. *Acta Crystallogr. Sect. C Struct. Chem.* **2015**, *71*, 3–8. [CrossRef]